Effect of In-Situ Ti$_2$N on Microstructure and Properties of SAF2906 Duplex Stainless Steel Fabricated by Laser Melting Deposition

Jing Liang[1] · Sheng Yang[1] · Ye Liu[1] · Xiuyuan Yin[1] · Suiyuan Chen[1] · Changsheng Liu[1]

Abstract

SAF2906 Duplex Stainless Steel (DSS) was fabricated by powder prepasted Laser Melting Deposition(LMD). The formation of ferrite was promoted by increasing the molybdenum content. The volume ratio of ferrite and austenite of LMDed SAF2906 DSS with 3 wt% molybdenum content reached 4:6. The effects of 2 wt% and 4 wt% nano TiN addition on the microstructure and comprehensive properties of LMDed SAF2906 DSS were investigated in detail. The results showed that in-situ generated nano (10 nm ~ 100 nm) and submicron (100 nm ~ 1 μm) Ti$_2$N particles were uniformly distributed in the LMDed SAF2906 DSS matrix, and some nano Ti$_2$N particles preferred to be distributed among grain boundaries. The primary and secondary dendrite spacing of austenite of LMDed SAF2906 with 4wt% TiN addition decreased by 48% and 62%, respectively, while the austenite content increased by 15%. The wear resistance, strength, elongation and corrosion resistance of the LMDed SAF2906 were gradually improved with the increase of nano TiN addition from 0 to 4 wt%. The average microhardness for the sample with 4 wt% nano TiN addition (381 HV$_{0.2}$) was 1.2 times that of the sample without TiN (326 HV$_{0.2}$), while the wear rate (9.12×10^{-13} m^3/Nm) was only 71% that of the sample without TiN (1.28×10^{-12} m^3/Nm). The yield strength, tensile strength and elongation of the LMDed SAF2906 with 4wt% TiN addition increased to 801 MPa, 1028 MPa and 31.8%, respectively. The self-corrosion potential increased to 0.0216 V, and the self-corrosion current density also reached 4.57×10^{-7} A·cm^{-2} for LMDed SAF2906 with 4wt% TiN addition.

1 Introduction

Duplex stainless steel (DSS) has excellent comprehensive performance, due to the combination of uniform corrosion resistance, high plasticity and weldability of austenitic stainless steels and the high strength and chloride stress corrosion resistance of ferritic stainless steels. SAF2906 is a kind of super duplex stainless steel with high content of chromium, molybdenum and nitrogen. The Pitting Resistance Equivalent Number (PREN) is greater than 42, and its strength is greater than 800 MPa, which is higher than that of SAF2205 (655 MPa) and SAF2507 (795 MPa). DSS is widely used in petrochemical, marine engineering, paper and pulp, energy and environmental protection and other fields [1, 2]. In particular, the impeller of the slurry pump in the phosphoric acid production is usually made of DSS. The balanced duplex volume ratio and microstructure of DSS are affected by the chemical composition and heat treatment process, so it is crucial to adopt appropriate manufacturing methods. DSS prepared by casting or forging was easy to precipitate secondary phases such as σ and Cr$_2$N, which drastically decreased the corrosion resistance and plasticity of the materials [3]. However, secondary phase precipitation mentioned above can be reduced or avoided during solidification with rapid cooling rate through laser melting deposition (about 10^5 K·s^{-1}) [4].

Laser Melting Deposition (LMD) is to use high-energy laser beam to rapidly melt metal powder and rapidly solidified, and then accumulate three-dimensional components layer by layer according to the design model. Parts with

✉ Jing Liang
liangj@atm.neu.edu.cn

1   Key Laboratory for Anisotropy and Texture of Materials, Ministry of Education, Key Laboratory for Additive Manufacturing and Remanufacturing Materials, School of Materials Science and Engineering, Northeastern University, Shenyang 110819, Liaoning, China

complex shapes and structures together with different sizes can be fabricated by LMD, with high material utilization and without molds. At present, LMD was mainly used in the preparation of 316L, 304 and other stainless steels [5–12]. Researches on additive manufacturing of DSS has just started in recent years and are still in their infancy. Laser Metal Deposition (LMD), Selective Laser Melting (SLM) and Wire Arc Additive Manufacturing (WAAM) have been used to fabricate DSS. Saeidi et al. [4] studied SAF2507 DSS manufactured by LMD, most of which were ferrite and only a small amount of austenite. The tensile strength, yield strength and microhardness of the LMDed SAF2507 were 1214 MPa, 1321 MPa and 450 HV respectively, which were superior to that of the conventional stainless steels. Hengsbach et al. [13] studied UNSS31803 DSS processed by SLM. The high cooling rate inhibited the nucleation of austenite, resulting in the almost entirely ferrite structure. After heat treatment, the volume ratio for austenite to ferrite was 3:7. K. P. Davidson et al. [14] prepared SAF2507 DSS by SLM. The average percentage of ferrite was 68.8%, and the ferrite grains grew along the building direction. The high cooling rate of SLM led to the precipitation of CrN and the maximum microhardness of the specimen was 449.4 HV, which was higher than that of the wrought substrate. With the increase of the laser energy input, the austenite percentage increased and the microhardness decreased. G. Posch et al. [15] used Cold Metal Transfer (CMT) as a heat source for WAAM to fabricate DSS 2209, which greatly reduced the heat input. So that no pore and improper fusion were found in the microstructure. An austenite/δ-ferrite weld microstructure with partly preferred grain orientations existed, and the δ-ferrite content was about 26~29%. The strength and toughness were equivalent to those of filler metals.

The production process of phosphoric acid is to extract the phosphoric acid in the phosphate rock with concentrated sulfuric acid. The impeller of the phosphoric acid slurry pump, as the key equipment, is used to transport the slurry. The impeller of the phosphoric acid slurry pump made of DSS is subjected to compound acid corrosion and wear of solid particles, so it is necessary to improve the impeller materials' wear resistance and corrosion resistance, and simultaneously meet certain mechanical performance requirements. Meanwhile, the impeller with complex shape is difficult to be formed, so it is essential to fabricate the impeller by LMD. To enhance corrosion resistance and wear resistance by fabricating the nano/submicron ceramic hard phases reinforced stainless steels became a research hotspot [16–18]. Titanium nitride (TiN) is a relatively stable ceramic

phase with high microhardness (21 GPa), high melting point (2950 °C), high chemical stability, good wear resistance and corrosion resistance [19, 20]. Many researchers have studied nano TiN/stainless steel composites. Wang et al. [21] studied nano TiN reinforced 316L composites prepared by LMD. When TiN addition increased from 0 to 6 wt%, the austenite dendrite spacing decreased from 11.2 μm to 3.5 μm, and TiN promoted the transformation of grains from columnar to equiaxed. The yield strength and tensile strength increased from 284 and 537 MPa to 457 MPa and 676 MPa, but the elongation decreased from 30 to 5% with TiN addition from 0 to 6 wt%. Oke et al. [22–25] and Ige et al. [26] studied nano TiN reinforced SAF2205 DSS composites fabricated by plasma sintering. TiN nanoparticles were uniformly distributed among the grain boundaries of the matrix, and the addition of TiN increased austenite content. The result of nano-indentation studies showed that as TiN addition increased from 0 to 8 wt%, the nano-hardness (from 4.9 to 19.4 GPa), elastic modulus (from 225 to 411 GPa), and the wear resistance were all improved. Olukayode Akinwamide et al. [27] studied nano TiN reinforced 304L composites by plasma sintering, and the sample with 4 wt% TiN addition had better resistance to chloride ion corrosion in 3.5 wt% NaCl solution.

In order to solve the problems that the impeller with complex shape was easy to be corroded and worn, and difficult to be formed, the SAF2906 DSS was fabricated by LMD, and the volume ratio of ferrite and austenite was adjusted by increasing molybdenum content. On this basis, SAF2906 DSS samples with different amount nano TiN additions were fabricated by LMD, and the effects of nano TiN addition on the microstructure and properties of SAF2906 DSS were studied.

2 Materials and Experimental Procedures

In this experiment, Q235 steel plates were selected as substrates. The 00Cr22Ni9 stainless steel powder, CrN powder and the corresponding Cr, Mo, Mn, Si, Cu, Fe element powders were used to prepare the SAF2906 DSS powder with nominal composition. The chemical composition of the 00Cr22Ni9 stainless steel powder used in the experiment and the SAF2906 powder mixture with the nominal composition were shown in Tables 1 and 2, respectively. The samples with 2 wt% and 3 wt% molybdenum contents were referred in the following text as SAF2906-2Mo and SAF2906-3Mo, respectively. The powder materials included

Table 1 The chemical composition of 00Cr22Ni9 stainless steel powder (wt%)

Elements	Cr	Ni	Mo	Mn	Cu	Si	C	N	Fe
00Cr22Ni9	23.10	9.74	3.22	1.04	0.018	0.29	0.009	0.00	Bal

Table 2 The chemical composition of SAF2906 powder mixture with nominal composition (wt%)

Elements	Cr	Ni	Mo	Mn	Cu	Si	C	N	Fe
SAF2906	29.00	6.00	2.00	0.81	0.79	0.72	0.009	0.30	Bal

spherical 00Cr22Ni9 stainless steel powder with the particle size of $50 \sim 150$ μm, Cr, Mo, Mn, Si, Cu elemental powders each with the particle size of ~ 75 μm, iron powder with the particle size of ~ 150 μm, and CrN powder of ~ 48 μm. CrN powder with the mass percentage of 9.86 wt%N was added in the powder mixture to obtain the 0.3 wt%N for the nominal composition of SAF2906.

2 wt% and 4 wt% nano TiN powder (~ 20 nm) was added to SAF2906-3Mo stainless steel powder mixture, and the samples with different TiN additions were referred as SAF2906-2TiN and SAF2906-4TiN in the following text, respectively. The powder mixture with different composition for SAF2906-2Mo, SAF2906-3Mo, SAF2906-2TiN and SAF2906-4TiN were mixed separately by a ball mill with a power of 250 W at a rotating speed of 270 rpm for 7.5 h. The SEM images of powder mixture were shown in Fig. 1. The powders were mixed evenly, and the nano TiN particles were uniformly distributed on the surface of stainless steel spherical powders (Fig. 1c–d).

The powder prepasted LMD process was carried out on Q235 substrates by using an FL-Dlight02-3000 W semiconductor laser processing system. Based on the previous experimental researches in the research group [28–30] and according to the formability assessment, defects observation and the single-path dimension, the process parameters were optimized (with the overlapping rate of 50%, laser power of 2100 W, scanning speed of 4.0 mm·s^{-1}, and interlayer waiting time of 2 min). A self-made special mold was used to ensure that the layer thickness was 0.3 ± 0.01 mm. The total thickness of LMDed specimen (40 mm $\times$ 25 mm) was 4.2 ± 0.01 mm after 14 layers were fabricated. The image of the final LMDed sample and the samples extracted for further microstructure observation and performance tests were shown in Fig. 2.

The LMDed samples were etched after grinding and polishing, and the etching solution was Beraha's reagent ($1g K_2S_2O_5 + 100$ mL(24 g(NH$_2$) HF$_2$ + 200mLHCl + 1000mLH$_2$O)). The microstructure and
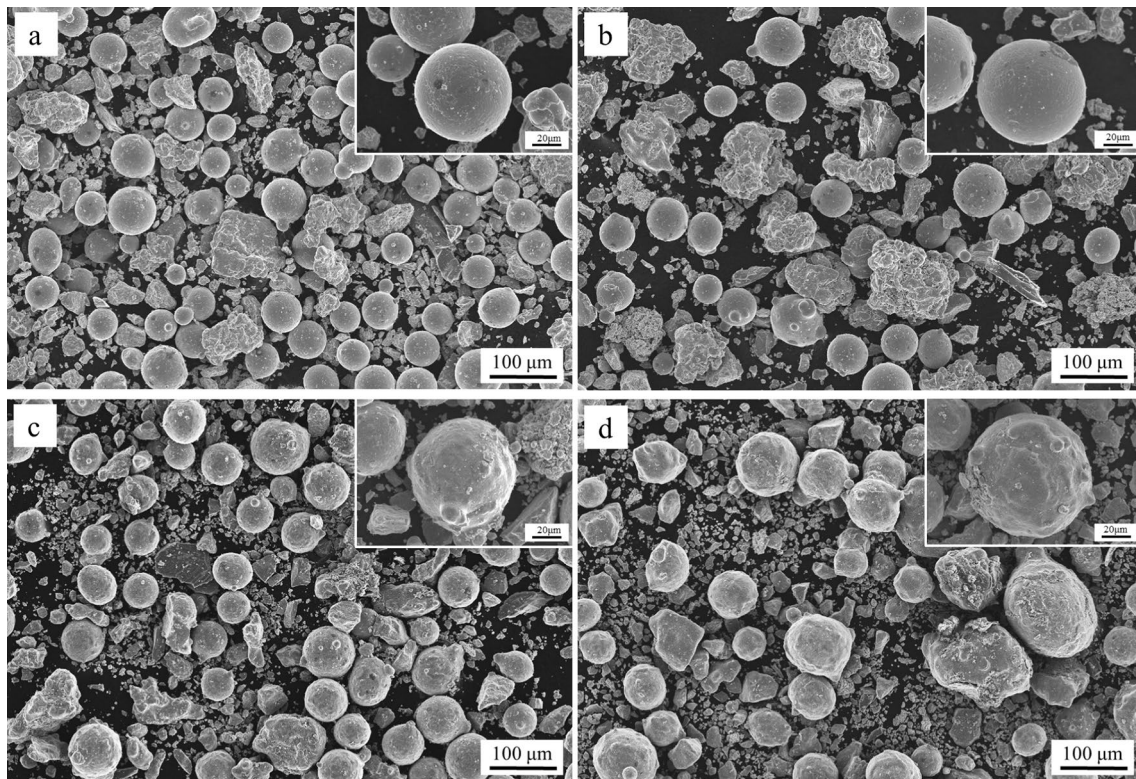

Fig. 1 SEM images of mixed powders with different molybdenum contents and nano TiN additions. **a** SAF2906-2Mo; **b** SAF2906-3Mo; **c** SAF2906-2TiN; **d** SAF2906-4TiN
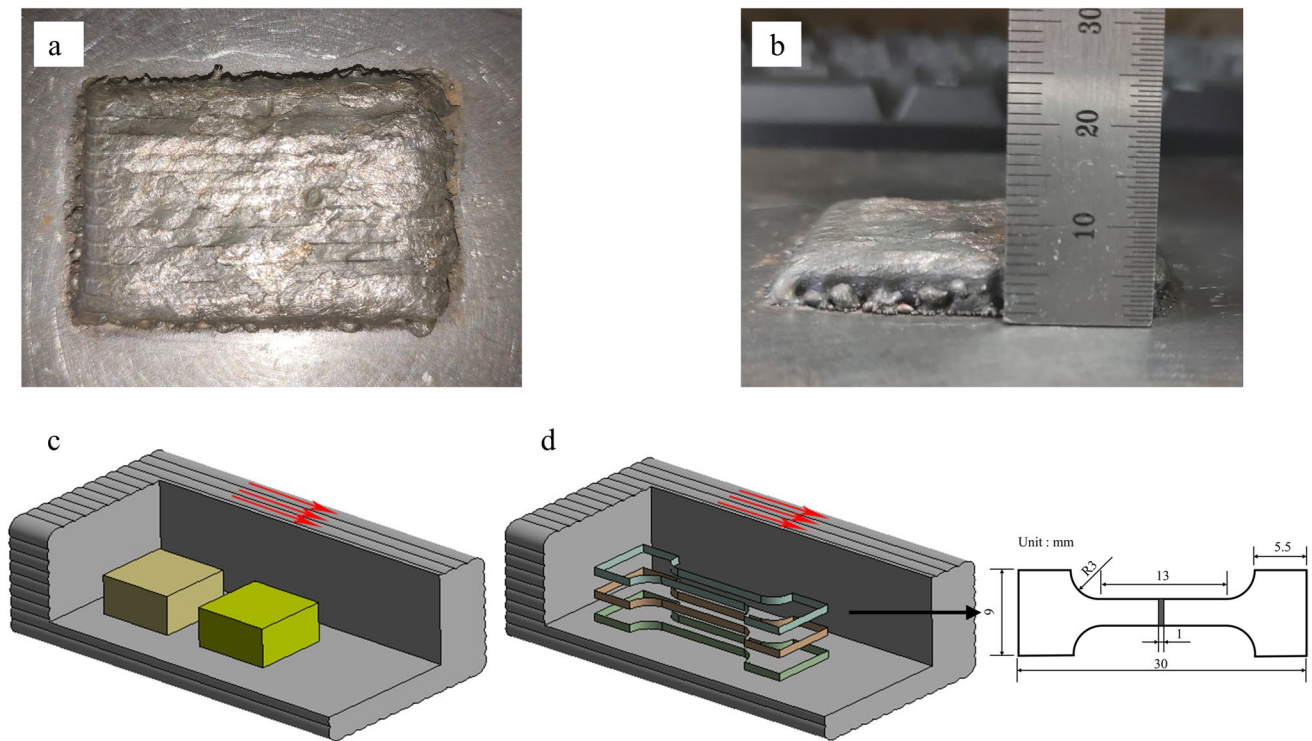
chemical composition of the samples were analyzed by an optical microscope (OLYMPUS-GX71), a Scanning Electron Microscope (SEM, Shimadzu-SSX-550) equipped with an Energy Dispersive Spectroscopy (EDS) and Field Emission Electron Probe Micro Analyzer system (EPMA, JXA-8530F) equipped with a Wavelength Dispersive Spectroscopy (WDS). The main phases were detected by an X-Ray Diffraction (XRD, PW3040/60) with Cu target K_α (with the tube voltage of 40 kV, the tube current of 200 mA, the scanning speed of $4°\cdot\text{min}^{-1}$ and the diffraction angle range from 30° to 100°). The samples were analyzed by a Transmission Electron Microscope (TEM, TECNAI G220).

The microhardness was tested by Wilson Wolpert 401MVD digital Vickers microhardness tester (with the load of 200 g, loading time for 10 s, and separation distance of 0.2 mm). The corrosion resistance was measured by the Coster CS350 test system (with the scanning speed of $0.5\ \text{mV}\cdot\text{s}^{-1}$ and scanning range from -0.8 to 0.8 V) in the $25\%\text{H}_3\text{PO}_4 + 2\%\text{H}_2\text{SO}_4 + 1\%\text{NaCl}$ aqueous solution. The sliding friction test was carried out by the American NANOVEA wear tester (with the load of 10 N, the speed of 200 $\text{r}\cdot\text{min}^{-1}$, and the wear time for 1 h). Tensile experiments were carried out using an AG-X100KN electronic universal material testing machine from Shimadzu, and the tensile speed was $0.5\ \text{mm}\cdot\text{min}^{-1}$.

3 Results and Analysis

3.1 Phase and Microstructure

Figure 3 showed the XRD results of the LMDed samples with different molybdenum contents and nano TiN additions and the volume fraction of ferrite and austenite calculated from intensities of different diffraction peaks in the XRD results. The LMDed samples all consisted of austenite(γ-Fe) and ferrite(α-Fe). The volume fraction of austenite for the LMDed SAF2906-2Mo sample was 74%, while the volume fraction of ferrite was only 26%. The imbalance between the two phases' volume fraction did not meet the requirement that the volume fraction of one phase in DSS should be at least 30%. Since molybdenum promoted the formation of ferrite, when the molybdenum content increased from 2 to 3 wt%, the intensity of ferrite diffraction peak at 2θ between 40° and 50° increased significantly for the SAF2906-3Mo sample, indicating the ferrite content effectively increased with the molybdenum content from 2 to 3 wt%, while the intensity of austenite diffraction peak between the same range decreased. The volume fraction for austenite of LMDed SAF2906-3Mo reduced to 57%, and the volume ratio of ferrite and austenite was about 4:6, which was an ideal volume ratio in DSS.
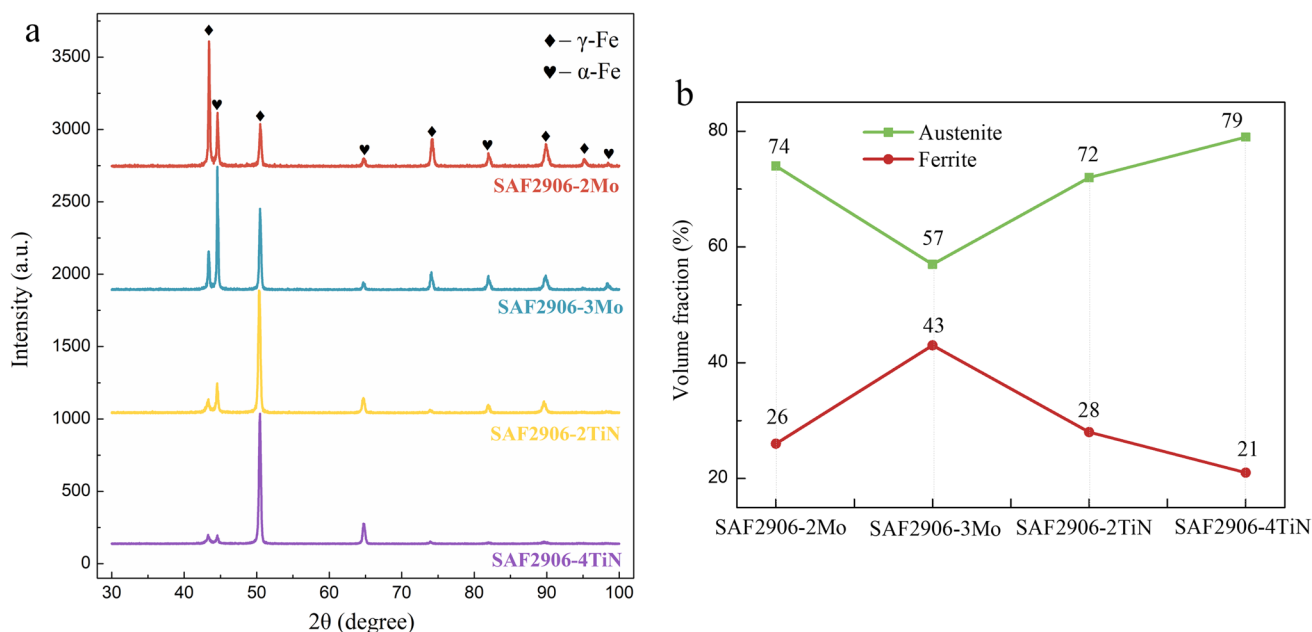
Fig. 3 **a** The XRD phase analysis of the LMDed samples with different molybdenum contents and nano TiN additions; **b** The volume fraction of ferrite and austenite of each sample calculated from intensities of diffraction peaks in the XRD results

Table 3 The 2θ of austenite(γ-Fe) of the LMDed SAF2906-3Mo samples with 0, 2, 4 wt% nano TiN additions (°)

Samples	SAF2906-3Mo	SAF2906-2TiN	SAF2906-4TiN
γ(111)	43.279	43.303	43.342
γ(200)	50.342	50.459	50.479
γ(220)	74.020	74.019	74.118
γ(311)	89.759	89.838	89.881

According to Fig. 3, with the increase of nano TiN addition (0, 2, 4 wt%), the intensity of austenite diffraction peak increased continuously, and no other phases except austenite and ferrite were detected in XRD results. For the LMDed SAF2906-2TiN sample, the austenite volume fraction increased sharply to 72%, and the volume ratio of ferrite and austenite was about 3:7. The austenite volume fraction of LMDed SAF2906-4TiN increased to 79%, and the volume ratio of the two phases was about 2:8. Table 3 showed the corresponding crystallographic plane angles of different crystal planes of austenite (γ-Fe) in the LMDed samples with different nano TiN additions. As the nano TiN addition increased from 0 to 4 wt%, the 2θ corresponding to the austenite peaks of different crystal planes shifted to the right to a certain extent, indicating that the corresponding interplanar spacing decreased according to the Bragg's Law $2d\sin\theta = n\lambda$. Since the nitrogen atomic radius is much smaller than that of iron, the dissolving of nitrogen in the iron matrix led to the increase in 2θ (that was the decrease in the crystal plane spacing). Since the instantaneous temperature of LMD for

the deposited layer reached the melting point of the nano TiN particles, TiN decomposed and nitrogen existed in the DSS matrix in the form of interstitial solid solution, promoting the formation of austenite. Therefore, the austenite content increased greatly in the LMDed samples with nano TiN addition.

Figure 4 was the low magnification OM image of SAF2906-3Mo. Beraha's reagent could darken ferrite and keep austenite white. The middle parts of all samples were composed of austenite and ferrite, in which austenite presented columnar dendritic structure and blocky structure. The primary dendrites of the columnar dendritic grains were thick and strong, and showed a certain direction. The blocky grains with uneven size were connected to each other. In the laser scanning formed molten pool, at the bottom of the single pass molten pool, the liquid metal near the fusion line was in contact with the solidified metal of the previous layer with fast heat dissipation, high cooling rate and large temperature gradient. Therefore, from the bottom of the molten pool along the direction of the temperature gradient, the solidified structure grew along the dendrites of the partially remelted grains of the previous deposition layer (Fig. 4b position 1) to form columnar dendrites (Fig. 4b position 2). At the same time, since the heat source was constantly moving during laser additive manufacturing, solidified structure grew at an angle along the scanning direction on the basis of the direction perpendicular to the previous layer of solidified metal. At the center and top of the single pass molten pool, the liquid metal was directly in contact with the air during the solidification and would be remelted when the next layer
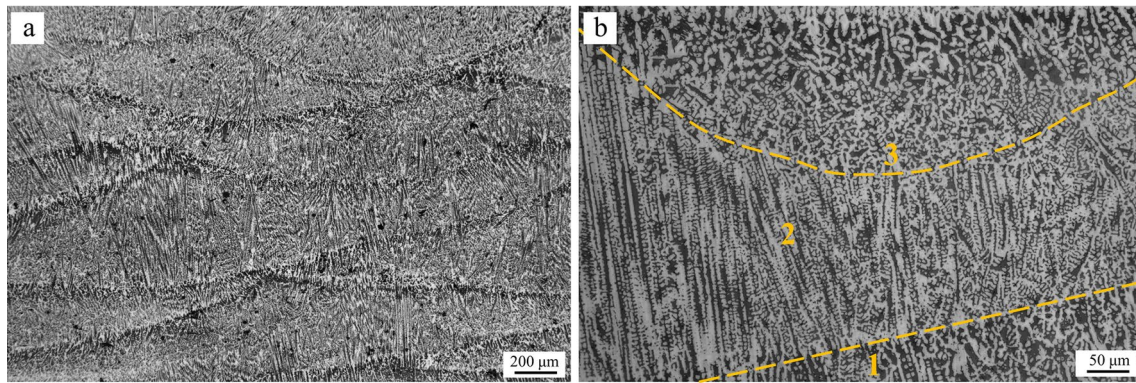
Fig. 4 The low magnification OM image of SAF2906-3Mo. **a** Morphology of multipass molten pool; **b** Morphology of single pass molten pool

was deposited. The heat dissipation condition of the metal was poor and the temperature gradient was narrow, so the growth mode of the metal changed to equiaxed grain growth (Fig. 4b position 3) [31].

Figure 5 showed the high magnification OM morphology and the distribution of the primary and secondary dendrite spacing of columnar dendritic austenite grains in the middle position of the LMDed samples with different molybdenum contents and nano TiN additions. Table 4 showed the proportion of austenite and ferrite of the LMDed samples with different molybdenum contents and nano TiN additions in Fig. 5a–d. The Image-Pro Plus software was used to measure the area of austenite and ferrite in the five OM images in the middle of the deposited sample, and calculate the proportion of the area of each phase to the total area. Then the average values were calculated to obtain the final proportion of austenite and ferrite. When molybdenum content increased from 2 to 3 wt%, the austenite content of columnar dendritic grains and blocky grains decreased significantly from 73 to 62%, while the ferrite content increased. The volume ratio of ferrite and austenite was about 4:6 for SAF2906-3Mo, which was basically consistent with the calculation based on XRD results in Fig. 3b. The increase of molybdenum promoted the formation of ferrite, so the ratio of the two phases was relatively balanced in the LMDed SAF2906-3Mo. The austenite content increased to 69% (for SAF2906-2TiN) and 77% (for SAF2909-4TiN) with the increase of TiN addition, respectively, shown in Fig. 5c and d. Nitrogen was dissolved into the matrix after TiN nanoparticles melted during the LMD process, which strongly promoted the formation of austenite.

The distance measurement function of Image-Pro Plus software was used to manually measure the primary and secondary dendrite spacing of austenite in five OM images. The primary dendrite spacing of austenite was 6.4 μm, while the secondary dendrite spacing was 2.1 μm for the LMDed SAF2906-3Mo sample (Fig. 5e, h). According to Fig. 5e–j, the dendrite spacing of austenite was significantly reduced with the addition of TiN. When the additions of TiN were

2 wt% and 4 wt%, the primary dendrite spacing reduced to 4.0 μm and 3.3 μm (Fig. 5f–g), while the secondary dendrite spacing decreased to 1.2 μm and 0.8 μm (Fig. 5i–j), respectively. Compared with the sample without TiN (SAF2906-3Mo), the primary and secondary dendrite spacings were reduced by 38% and 43% (SAF2906-2TiN), and 48% and 62% (SAF2906-4TiN), respectively, suggesting that the microstructure was obviously refined.

Figure 6 showed the SEM images of the middle position of the LMDed samples with different molybdenum contents and nano TiN additions, and the high-magnification SEM images of the reinforced particles in the LMDed SAF2906-4TiN. Table 5 showed the results of the spot analysis of EPMA at different positions in Fig. 6a–d. Table 5 showed that the dark gray area (position 1 in Fig. 6a, position 3 in Fig. 6b, position 5 in Fig. 6c, position 7 in Fig. 6d) with high content of molybdenum and the low content of nickel was the ferrite phase, while the light grey area (position 2 in Fig. 6a, position 4 in Fig. 6b, position 6 in Fig. 6c, position 8 in Fig. 6d) with high content of nickel and the low content of molybdenum was the austenite phase. The reinforced particles in the LMDed SAF2906-2TiN and SAF2906-4TiN samples were uniformly distributed in the DSS matrix, shown in Fig. 6c and d. With the increase of nano TiN addition, the number of reinforced particles increased. According to Fig. 6e and f, the reinforced particles were mainly in quadrilateral and spherical shapes, due to the observation from each side in different orientation.

According to Table 5, during the process of LMD, there was a certain amount of burning loss and segregation of each element. As it can be seen from Table 5, the molybdenum content of the LMDed SAF2906-2Mo sample was only about 1 wt% (position 1, 2 in Fig. 6a), which was lower than the nominal molybdenum content of SAF2906 (1.5–2.5 wt%), thus the burning loss reached about 1 wt%. The molybdenum content of the SAF2906-3Mo sample reached 2 wt% (position 3, 4 in Fig. 6b), which was within the standard range, then leading the volume ratio of ferrite
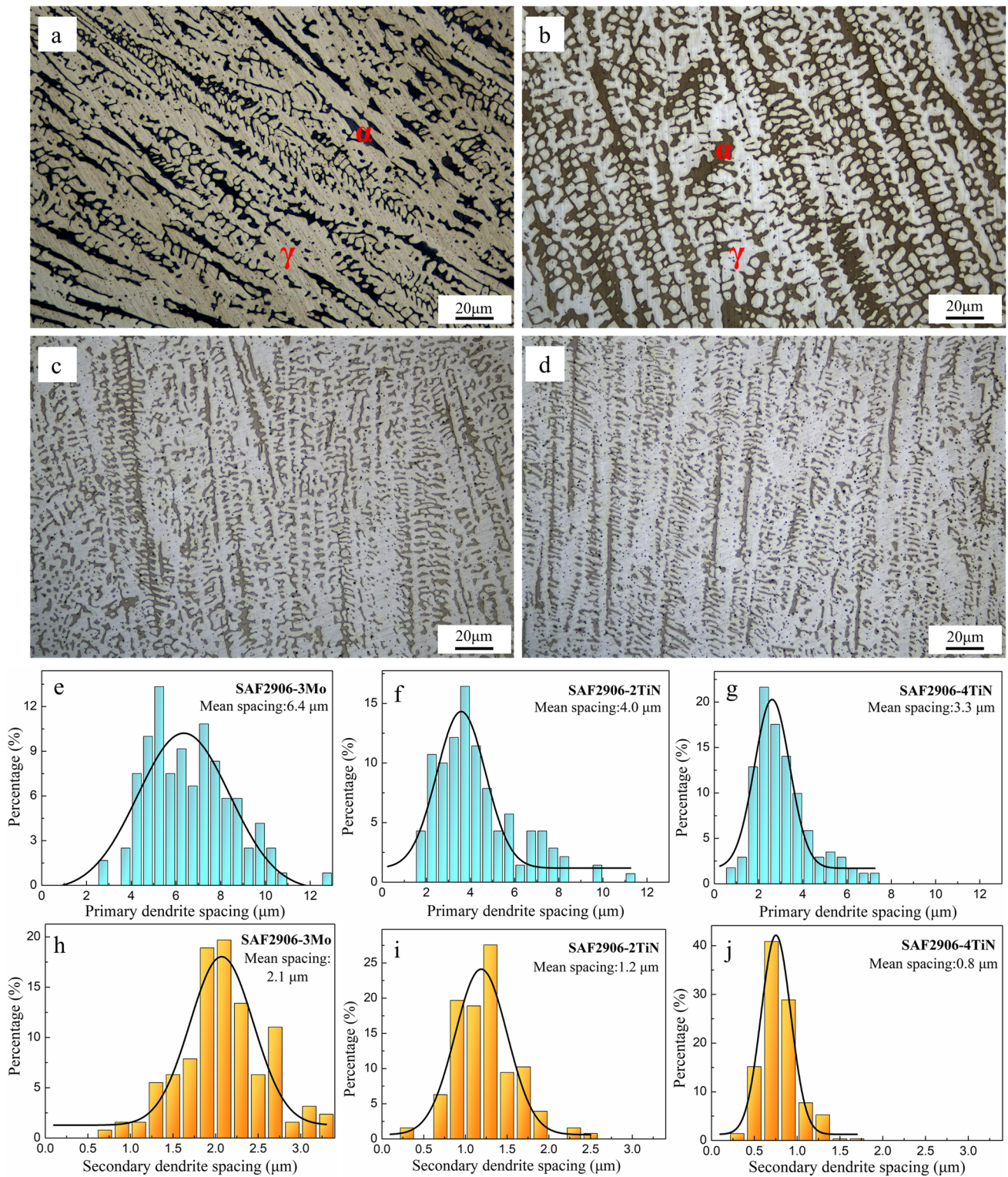
Fig. 5 **a–d** The OM morphology of SAF2906-2Mo, SAF2906-3Mo, SAF2906-2TiN and SAF2906-4TiN; **e–g** The distribution of primary dendrite spacing of columnar dendritic austenite grains of SAF2906-3Mo, SAF2906-2TiN and SAF2906-4TiN; **h–j** The distribution of secondary dendrite spacing of SAF2906-3Mo, SAF2906-2TiN and SAF2906-4TiN

Table 4 The proportion of austenite and ferrite of the LMDed SAF2906 with different molybdenum contents and nano TiN additions calculated by the Image-Pro Plus software (%)

Samples	Austenite(γ)	Ferrite(α)
SAF2906-2Mo	73	27
SAF2906-3Mo	62	38
SAF2906-2TiN	69	31
SAF2906-4TiN	77	23

and austenite of LMDed SAF2906-3Mo to reach a relatively ideal value (about 4:6). With the addition of TiN increasing from 0 to 2 wt%, the nitrogen content of the matrix rose from 0.2 wt% (at position 4 in Fig. 6b) to 0.8 wt% (at position 6 in Fig. 6c), indicating that nitrogen was dissolved in the iron matrix, which promoted the formation of austenite and played a role in solid solution strengthening to improve the strength of the material. The matrix contained almost no titanium element (at positions 1–8 in Fig. 6a–d), indicating that most titanium existed in the reinforced particles.
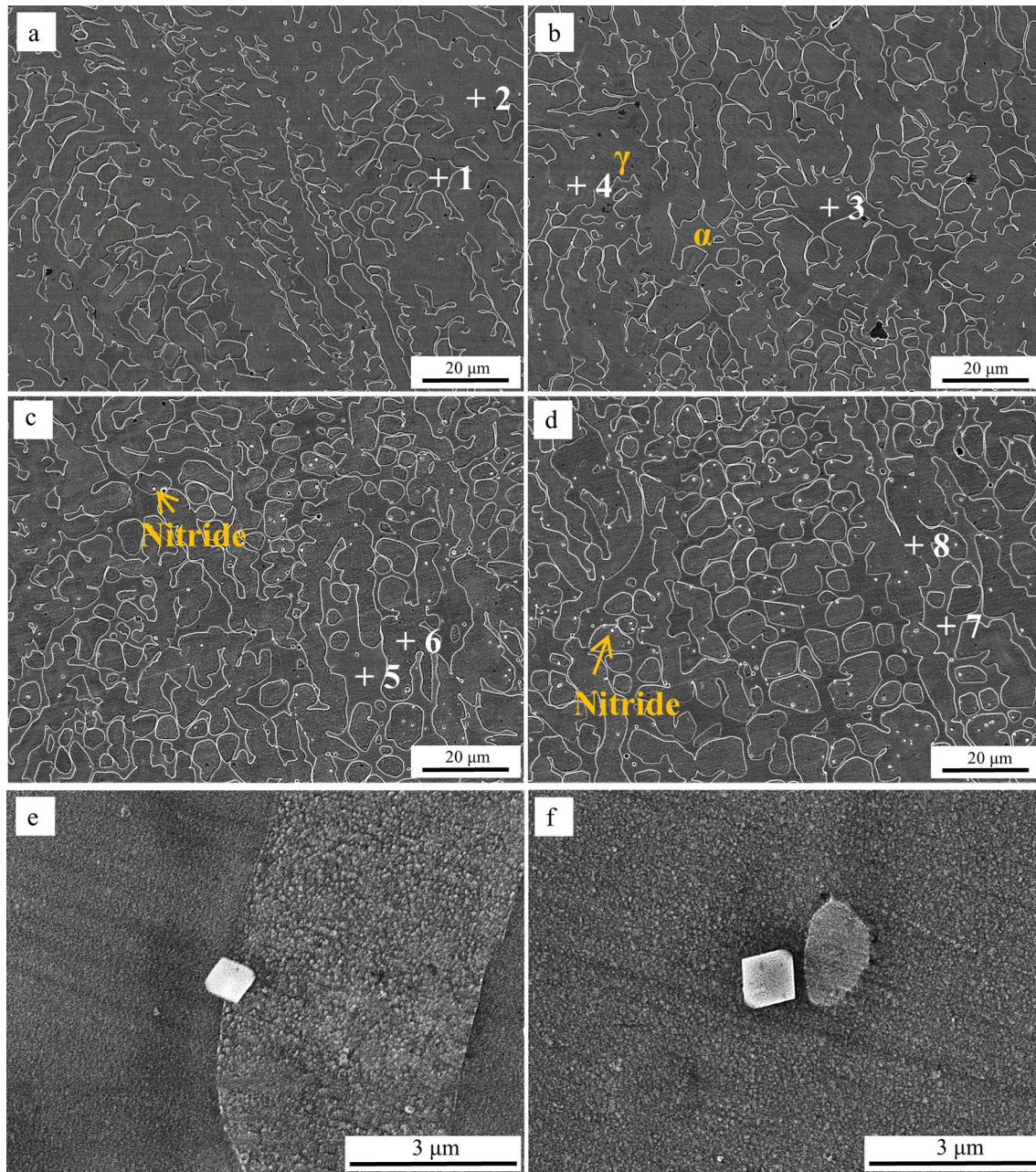

Fig. 6 The SEM images of the LMDed samples with different molybdenum contents and nano TiN additions. **a** SAF2906-2Mo; **b** SAF2906-3Mo; **c** SAF2906-2TiN; **d** SAF2906-4TiN; **e–f** The reinforced particles in the LMDed SAF2906-4TiN sample

Table 5 The results of the spot analysis of EPMA at different positions in Fig. 6a–d (wt%)

Elements	Cr	Ni	Mo	N	Ti
1	25.418	4.267	1.055	0.055	0.000
2	25.546	6.602	1.146	0.219	0.000
3	26.358	3.740	2.119	0.000	0.000
4	26.923	6.680	1.757	0.206	0.000
5	27.379	5.339	1.999	0.169	0.000
6	29.020	6.841	1.616	0.856	0.008
7	26.819	4.603	1.956	0.000	0.069
8	26.942	6.370	1.292	0.934	0.002

Figure 7a showed the TEM image of austenite and ferrite structure of DSS. There existed the interphase distribution of austenite and ferrite phase. Figure 7b–e showed the images and diffraction pattern of the in-situ generated reinforced particles. According to the TEM-EDS mapping results shown in Fig. 8, titanium and nitrogen were enriched in the reinforced particle. Table 6 showed the TEM-EDS point analysis results of the reinforced particle of LMDed SAF2906-4TiN in Fig. 7b position A and B. The reinforced particle was almost all composed of titanium and nitrogen elements, and the content of titanium was much higher than that of nitrogen (Fig. 7b position A). The reinforced particle was determined to be Ti_2N by TEM diffraction pattern
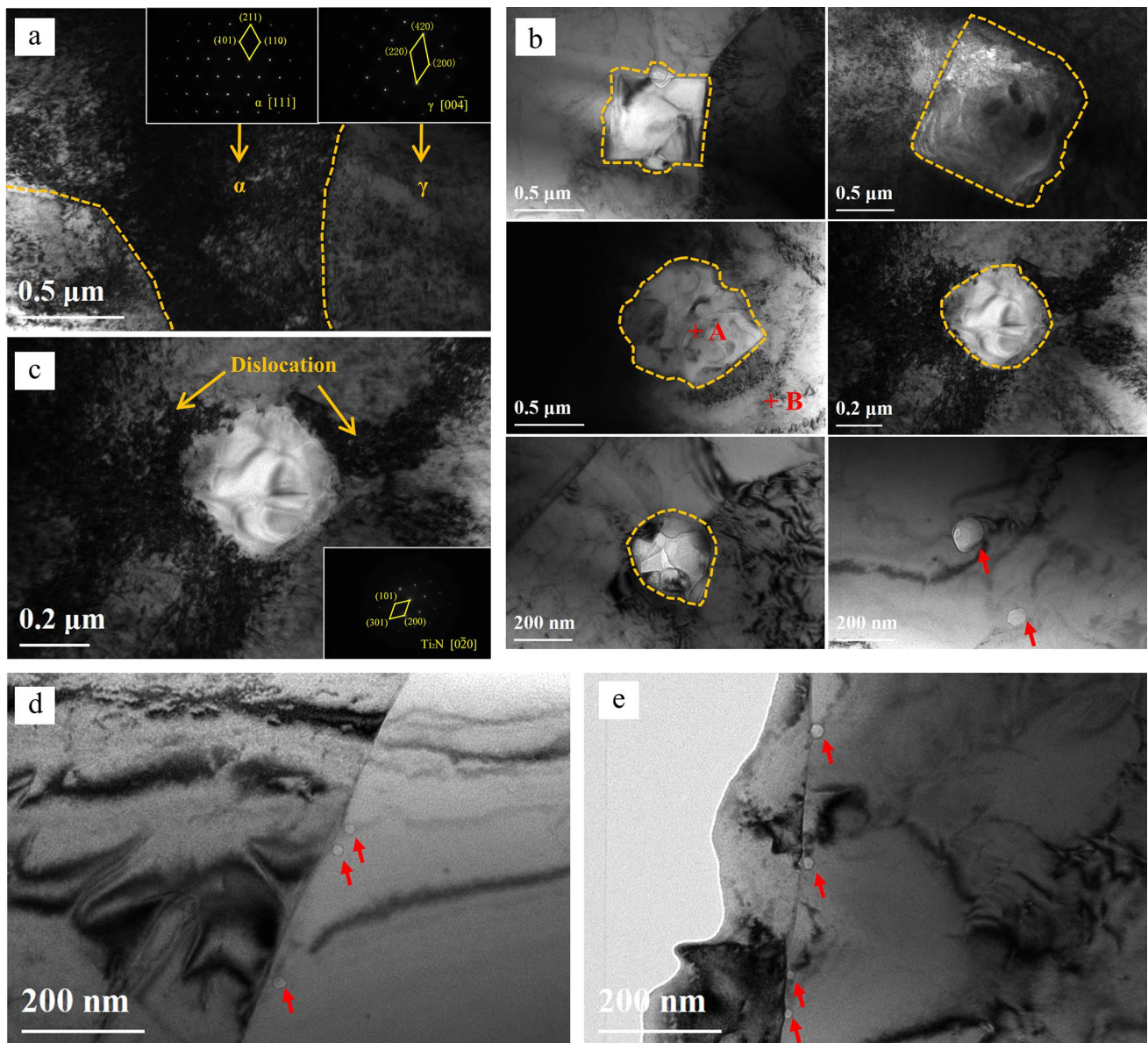

Fig. 7 The TEM images of LMDed SAF2906-4TiN and the diffraction pattern for each phase. **a** Matrix: austenite and ferrite; **b** The morphology of reinforced particles; **c** The electron diffraction pattern of reinforced particle; **d–e** Nano Ti_2N particles distributed among grain boundaries

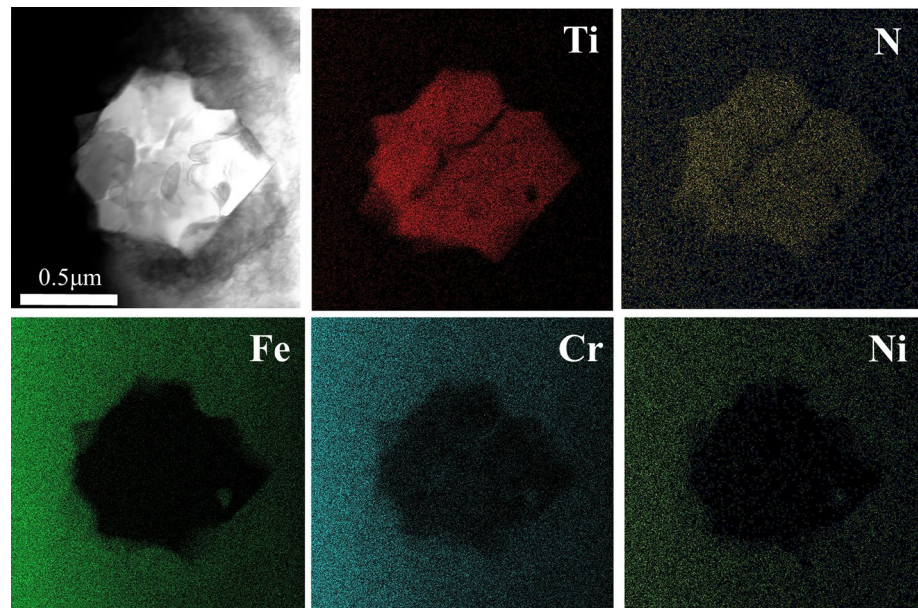**Fig. 8** TEM-EDS elemental mapping of reinforced particle of the LMDed SAF2906-4TiN

Table 6 TEM-EDS results of the reinforced particle of LMDed SAF2906-4TiN in Fig. 7b (at%)

Elements	N	Ti	Cr	Fe	Ni	Mo	Mn	Si
A	19.28	70.41	0.19	5.28	0.28	0.17	4.02	0.37
B	0.4	0.03	30.67	59.40	5.84	1.76	0.45	1.09

(Fig. 7c). These in-situ Ti_2N particles were mainly quadri-lateral and spherical, with size ranging from 100 nm to 1 μm as the submicron structure and 10 nm ~ 100 nm as the nano structure. The laser rapid forming made the instantaneous temperature of the deposited layer reach the melting point of the nano TiN particles, and then nitrogen and very little titanium were dissolved into the iron-based matrix during solidification. Nitrogen with the small atomic radius was dis-solved into γ-Fe to form the interstitial solid solution, while titanium with the large atomic radius was dissolved into α-Fe to form the substitutional solid solution. Meanwhile, when the temperature during LMD was about 1000–3000 °C, the diffusion coefficient of nitrogen in liquid iron (about $8.45 \times 10^{-4} \sim 9.32 \times 10^{-4}$ $cm^2 \cdot s^{-1}$) was much larger than that of titanium in liquid iron (about $5.86 \times 10^{-6} \sim 8.64 \times 10^{-5}$ $cm^2 \cdot s^{-1}$) [32], so nitrogen diffused faster into the iron matrix under the same condition compared with titanium. During the subsequent rapid cooling and solidification, the remain-ing larger amount of titanium combined with nitrogen to in situ form Ti_2N reinforced particles with nano and sub-micron size. Further observation of Fig. 7c showed that there were high-density dislocations distributed around the Ti_2N particles, indicating that the reinforced Ti_2N particles effectively pined dislocations and hindered the movement of dislocations, thereby improving the strength of the mate-rial. The in-situ nano Ti_2N particles usually pinned at grain boundaries (Fig. 7d, e) and hindered the growth of grains,

while in-situ submicron Ti_2N particles supplied effective heterogeneous nucleation, resulting in effective refinement of austenite grains to 3.3 μm (Fig. 5g).

3.2 Comprehensive Properties

3.2.1 Microhardness and Wear Resistance

Figure 9 showed the microhardness of the LMDed samples with different molybdenum contents and nano TiN additions. The average microhardness of SAF2906-3Mo changed less compared to SAF2906-2Mo, rising from 319 $HV_{0.2}$ to 326 $HV_{0.2}$. With the increase of molybdenum content, molyb-denum was dissolved into the stainless steel matrix to form substitutional solid solution. The atomic radius of molyb-denum was larger than that of iron, which caused a certain lattice distortion in the matrix lattice to achieve the solid solution strengthening, which was beneficial to the improve-ment of microhardness.

The microhardnesses of SAF2906-2TiN and SAF2906-4TiN were significantly higher than that of the SAF2906-3Mo without nano TiN addition. When nano TiN addition increased from 0 to 2 wt% and 4 wt%, the average micro-hardness increased from 326 $HV_{0.2}$ to 361 $HV_{0.2}$ and 381 $HV_{0.2}$. Part of nitrogen was dissolved into the iron matrix to form the interstitial solid solution, resulting in lattice distortion and strong solid solution strengthening effect.
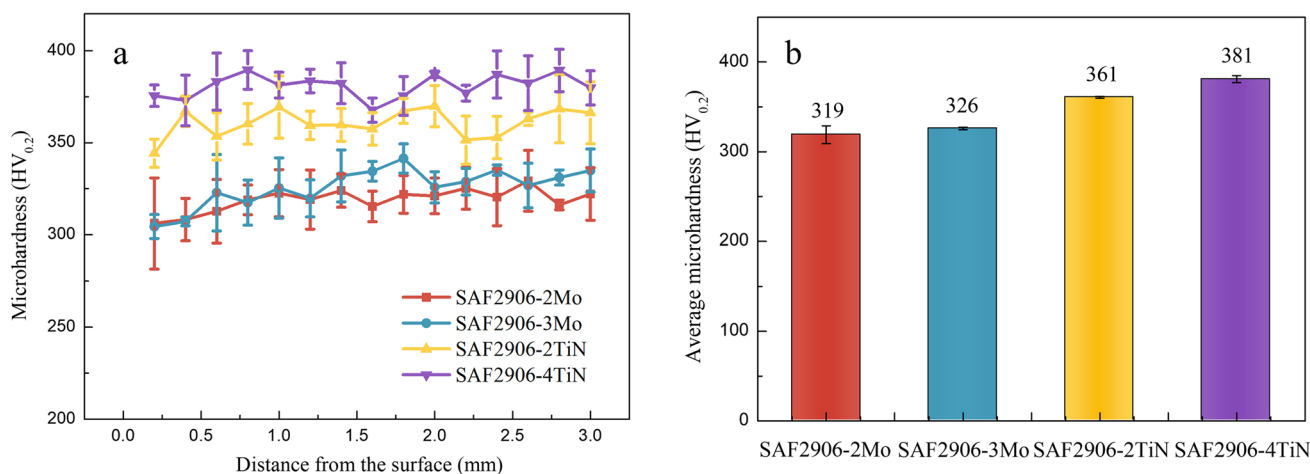
Fig. 9 The microhardness of the LMDed samples with different molybdenum contents and nano TiN additions. **a** Microhardness distribution along the deposition direction; **b** Average microhardness

Meanwhile, there were also the precipitation strengthening and the fine grain strengthening effects of in-situ Ti_2N particles to improve the microhardness of the samples with nano and submicron Ti_2N particles.

Figure 10a showed the coefficient of friction curves of the LMDed SAF2906 with different molybdenum contents and nano TiN additions, and the average coefficients of friction and wear rate were shown in Fig. 10c–d, respectively. The assumptions of the friction and wear tests were that the contact pressure between the sample and the wear ball was uniform and the applied load was constant during the friction and wear process.

Generally, wear rate is used to express the wear resistance of materials. The smaller the wear rate, the better the wear resistance of materials. In this experiment, the wear volume(V) was calculated by formula (1), and the wear rate(k) was calculated by formula (2).

$$V = \frac{Lh\left(3h^2 + 4b^2\right)}{6b} \tag{1}$$

$$k = \frac{V}{PS} \tag{2}$$

where V was the wear volume (m^3); L was the length of wear scar (m); h was the depth of wear scar (m); b was the width of wear scar (m). The above data were detected by confocal laser scanning microscope. k was the wear rate (m^3/Nm); P was the load (N); S was the total sliding distance (m).

When the molybdenum content increased from 2 to 3 wt%, the average coefficient of friction decreased slightly from 0.5967 to 0.5885 (Fig. 10c), and the wear rate decreased from 1.77×10^{-12} m^3/Nm to 1.28×10^{-12} m^3/Nm (Fig. 10d), indicating that the appropriate increase of molybdenum

content was beneficial to improve the wear resistance of the samples. The coefficient of friction curves of SAF2906-2TiN and SAF2906-4TiN were significantly lower than that of the SAF2906-3Mo sample (Fig. 10a). The average coefficient of friction reduced from 0.5885 (SAF2906-3Mo) to 0.5382 (SAF2906-2TiN) and 0.5492 (SAF2906-4TiN), and the wear rate decreased from 1.28×10^{-12} m^3/Nm (SAF2906-3Mo) to 9.99×10^{-13} m^3/Nm (SAF2906-2TiN) and 9.12×10^{-13} m^3/Nm (SAF2906-4TiN), with wear rate decline by 29% (Fig. 10c–d). Simultaneously, it can be seen from the section profiles of the wear track in Fig. 10b that the wear depth of SAF2906-4TiN (47.56 μm) was minimal, which were about 13 μm smaller than that of SAF2906-3Mo (60.01 μm). The wear resistance was improved after adding nano TiN to the DSS and then forming Ti_2N reinforced composites.

Figure 11 and Table 7 showed the SEM images and EDS results of the wear surface of the LMDed samples with different molybdenum contents and nano TiN additions. Wear debris, spalling pits and grooves appeared on the wear surface of the samples, shown in Fig. 11b, d, f and h. For the SAF2906-2Mo and SAF2906-3Mo samples (Fig. 11b, d), during the friction and wear process, the stainless steel material and the friction pair (Al_2O_3 ball with a diameter of 6 mm) continued to slide and rub back and forth, and the surface material cannot withstand more dislocations and formed cracks, eventually causing the surface material to fall off and form spalling pits (Fig. 11b, d). In the process of repeated friction and wear, the granular materials falling off the surface continuously re-embedded in the wear surface of the sample. The material further deformed under the action of friction, and the surface tearing occurred, leading to plastic deformation (Fig. 11b, d) caused by extrusion in the deeper part of the grooves. Analysis of the EDS results (Table 7) showed
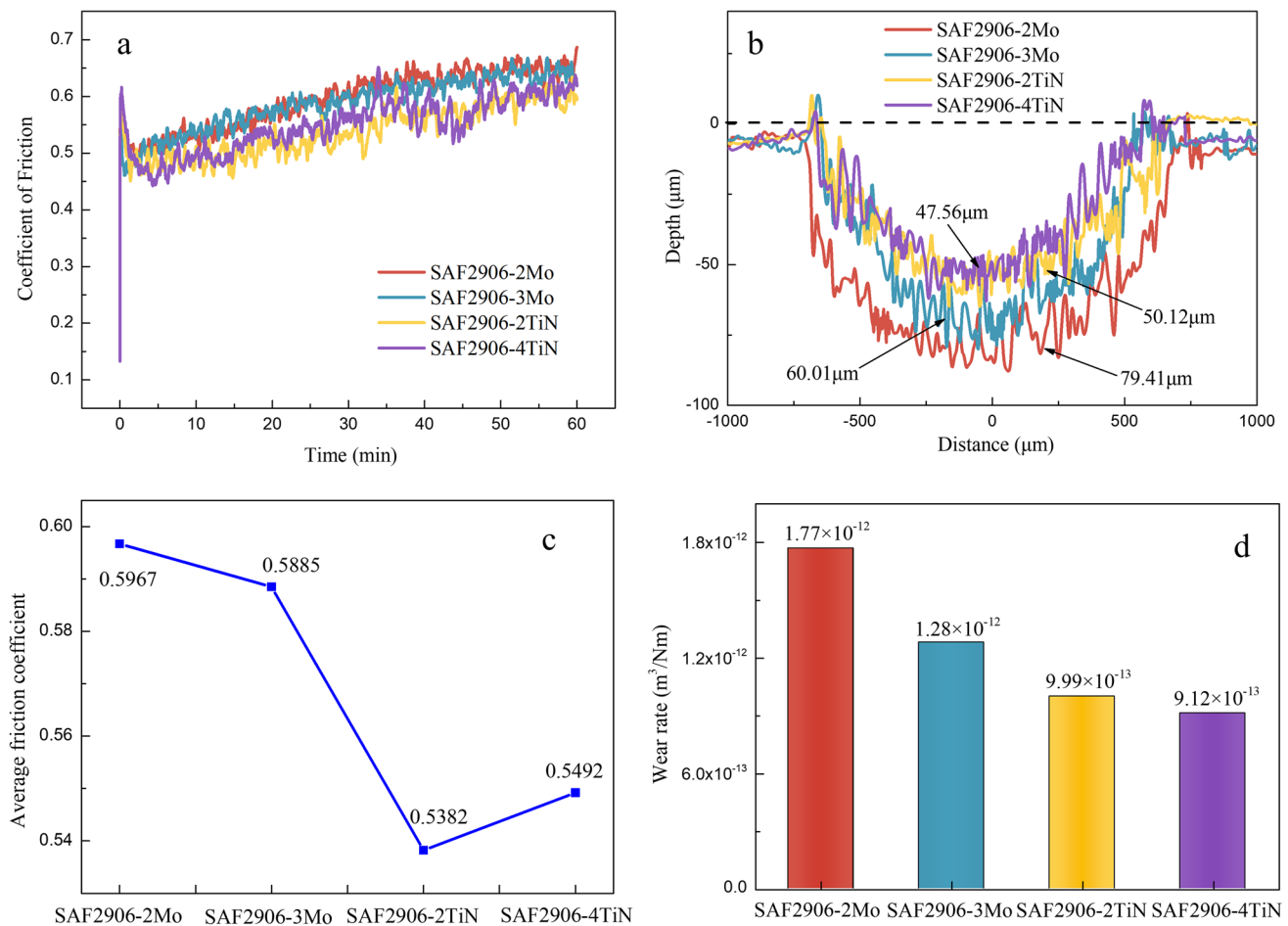
Fig. 10 **a** Coefficient of friction curves; **b** The section profiles of the wear track; **c** Average coefficients of friction; **d** Wear rate of the LMDed samples with different molybdenum contents and nano TiN additions

that the aluminum and oxygen elements at position 1 in Fig. 11d were high, but they were not enriched at position 2 in Fig. 11d, indicating that the aluminum and oxygen elements in the Al_2O_3 balls were transferred to the exfoliates during the friction and wear process, forming adhesive traces. Meanwhile, the temperature rose during the friction and wear process caused the aluminum element reacting with oxygen to form oxide abrasive debris. The wear mechanisms of the LMDed SAF2906-2Mo and SAF2906-3Mo were abrasive wear and adhesive wear.

Compared with SAF2906-2Mo and SAF2906-3Mo (Fig. 11a, c), the width of wear traces of SAF2906-2TiN and SAF2906-4TiN (Fig. 11e, g) were obviously smaller. No obvious plastic deformation was observed on the wear surface of the SAF2906-2TiN and SAF2906-4TiN (Fig. 11f, h). The wear debris and spalling pits were significantly reduced, and the surfaces were flat with only slight grooves (Fig. 11f, h) compared with SAF2906-3Mo (Fig. 11d), indicating better wear resistance obtained for the two samples with TiN addition. The wear mechanisms of the LMDed

SAF2906-2TiN and SAF2906-4TiN were also abrasive wear and adhesive wear.

The material with high microhardness was highly resistant to plastic deformation and wear. The samples without Ti_2N with lower microhardness (Fig. 9) were easy to be worn under the action of external force. However, the in-situ generated nano and submicron Ti_2N particles were ceramic reinforced phases with high microhardness, and its microhardness was much higher than that of the stainless steel matrix, so they greatly improved the microhardness of the composites. Due to the huge difference in microhardness between stainless steel matrix and Ti_2N hard particles, there was obvious selectivity in the wear test. The initial wear was mainly carried out on the DSS matrix with flat surface, and the DSS matrix was worn. When the DSS matrix was worn to a certain extent, the Ti_2N particles were slightly raised, which made the surface height of the matrix correspondingly lower than that of the Ti_2N hard particles. The Ti_2N particles were slightly convex on the worn surface, forming a hard skeleton. When the load was directly applied to the convex
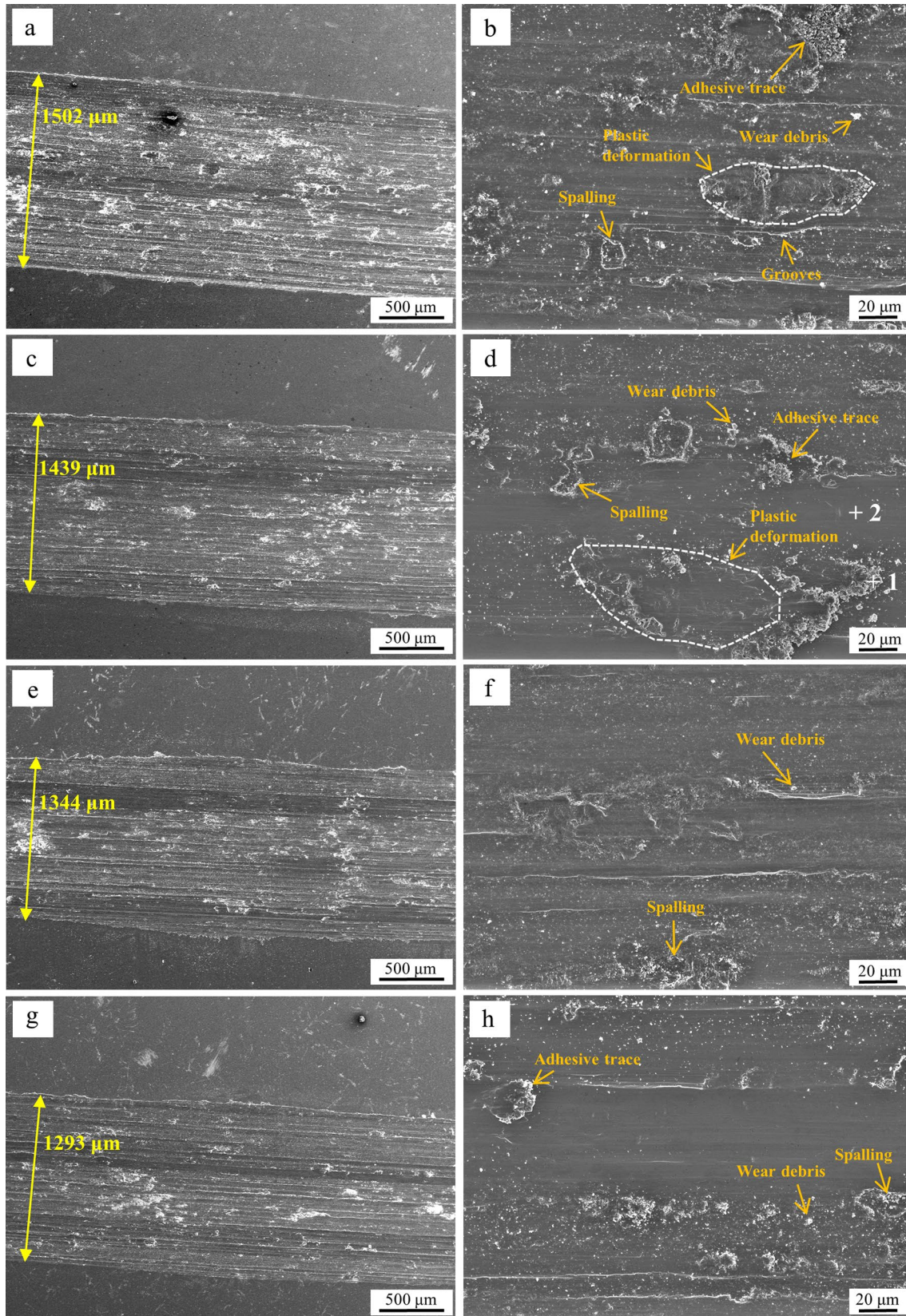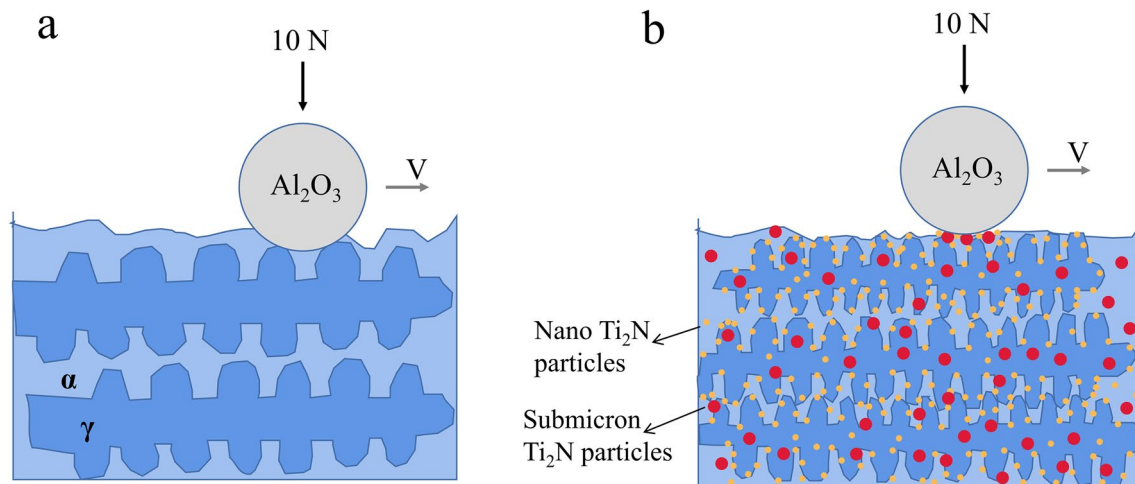
Fig. 11 The low and high magnification SEM wear surface images of the LMDed samples with different molybdenum contents and nano TiN additions. **a–b** SAF2906-2Mo; **c–d** SAF2906-3Mo; **e–f** SAF2906-2TiN; **g–h** SAF2906-4TiN

Table 7 SEM–EDS results of morphologies of different positions in Fig. 11d (wt%)

Elements	Al	O	Cr	Fe	Ni	Mo
1	1.36	21.99	19.73	48.28	4.18	2.22
2	0.00	0.00	26.97	64.30	6.09	2.63


Fig. 12 The wear mechanisms of the LMDed samples. **a** Samples without Ti$_2$N; **b** Samples with nano and submicron Ti$_2$N

particles, Ti$_2$N particles played a main supporting role during the process of wear contact and reduced the actual contact area between the friction ball and the material[33], weakening the plastic deformation of the matrix and protecting the materials from serious wear, shown in Fig. 12. When the surface of Ti$_2$N particles was worn to the same plane as the matrix, the wear continued to the DSS matrix material. This situation occurred alternately, which inevitably reduced the wear on the stainless steel matrix material and improved the wear performance of the composites.

3.2.2 Mechanical Properties

Figure 13 showed the tensile stress–strain curves of the LMDed samples with different molybdenum contents and nano TiN additions, and Table 8 listed the corresponding yield strength, tensile strength and elongation of different samples. Compared with SAF2906-3Mo, the yield strength, tensile strength and elongation gradually increased with the increase of nano TiN addition. The yield strength and tensile strength of SAF2906-4TiN sample increased from 700 and 885 MPa (for SAF2906-3Mo) to 801 MPa and 1028 MPa, respectively. The elongation of SAF2906-4TiN sample greatly improved from 16.9% (for SAF2906-3Mo) to 31.8%.

After adding nano TiN particles to SAF2906-3Mo, the in-situ generated nano and submicron Ti$_2$N reinforced particles were uniformly dispersed in the DSS matrix (Fig. 6c–d), and some nano Ti$_2$N particles preferred to be distributed among grain boundaries (Fig. 7d–e). The nano Ti$_2$N hard
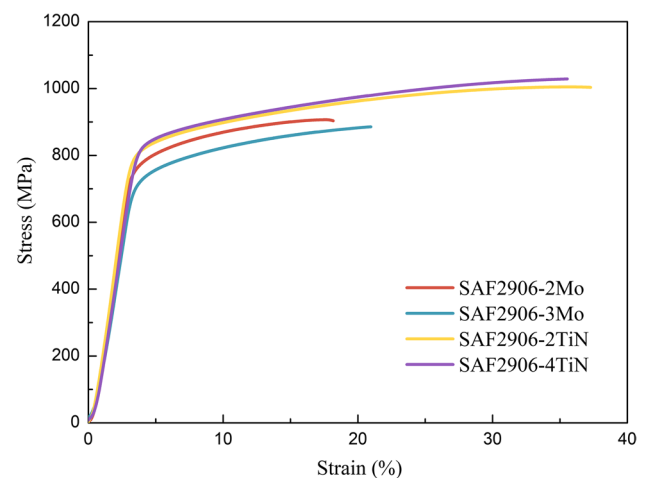
Fig. 13 The tensile stress–strain curves of the LMDed samples with different molybdenum contents and nano TiN additions

particles produced the pinning effect of grain boundaries and hindered the growth of grains, while submicron Ti$_2$N particles supplied effective heterogeneous nucleation, resulting in refinement of the grains, which played a role in fine grain strengthening according to the Hall–Petch relationship. In addition, nitrogen was dissolved into the austenite lattices (Table 5) to form interstitial solid solution, and the lattice distortion was generated near the nitrogen atom to form the stress field. The stress field interacted with dislocations and hindered the movement of dislocations, playing a role in

Table 8 Mechanical properties of the LMDed samples with different molybdenum contents and nano TiN additions

Samples	Yield strength /MPa	Tensile strength /MPa	Elongation/%
SAF2906-2Mo	722 ± 9.2	906 ± 12.0	14.3 ± 0.4
SAF2906-3Mo	700 ± 4.2	885 ± 3.5	16.9 ± 1.7
SAF2906-2TiN	779 ± 21.2	1005 ± 23.3	32.1 ± 1.2
SAF2906-4TiN	801 ± 7.07	1028 ± 15.5	31.8 ± 2.6

solid solution strengthening. Furthermore, according to the Orowan strengthening mechanism, when the dislocation line encountered the nano and submicron Ti_2N particles, the dislocation line bypassed the reinforced particles or bent along the reinforced particles, forming the dislocation loop and then hindering the dislocation movement, which resulted in the strengthening of the material. So under the main effects of Orowan strengthening, solid solution strengthening and fine grain strengthening, the strength of composites was improved.

The SEM images of the tensile fracture surface of the LMDed samples with different molybdenum contents and nano TiN additions were shown in Fig. 14. Figure 15 showed the tensile fracture mechanism of the LMDed samples. There were continuous dimples at the fracture surfaces of all samples (Fig. 14a–d), which was the typical characteristics of ductile fracture. In the samples without nano TiN addition, a very small amount of dimples contained unmelted inclusions (Fig. 14a–b), while the SAF2906-2TiN and SAF2906-4TiN samples had few similar inclusions, and the dimples were more uniform and dense (Fig. 14c–d). The laser absorption rate of stainless steel (about 20%) was much smaller than that of the ceramic phase (about 90%) [34, 35], so there was a small amount of inclusions in the samples without the ceramic phase (Fig. 14a–b). A small amount of unmelted inclusions destroyed the continuity of the duplex stainless steel matrix and became a weak area in the tensile fracture process. During the tensile process, stress concentration was generated at the junction of inclusions and the matrix, resulting in uneven deformation and tiny holes. As the tensile deformation proceeded, inclusions debonded with the stainless steel matrix, making the tiny pores develop into microcracks and accelerate the fracture (Fig. 15a). Finally, the strength and elongation of the material were reduced.
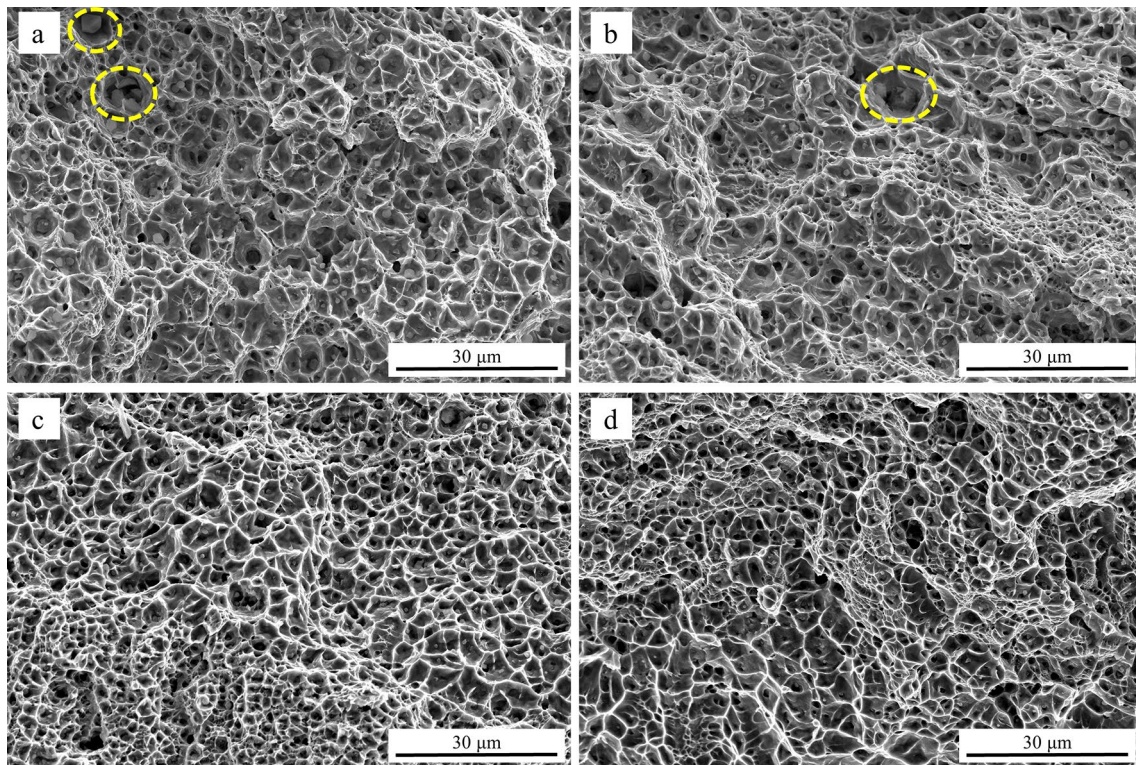

Fig. 14 The SEM images of the tensile fracture surface of the LMDed samples with different molybdenum contents and nano TiN additions. **a** SAF2906-2Mo; **b** SAF2906-3Mo; **c** SAF2906-2TiN; **d** SAF2906-4TiN
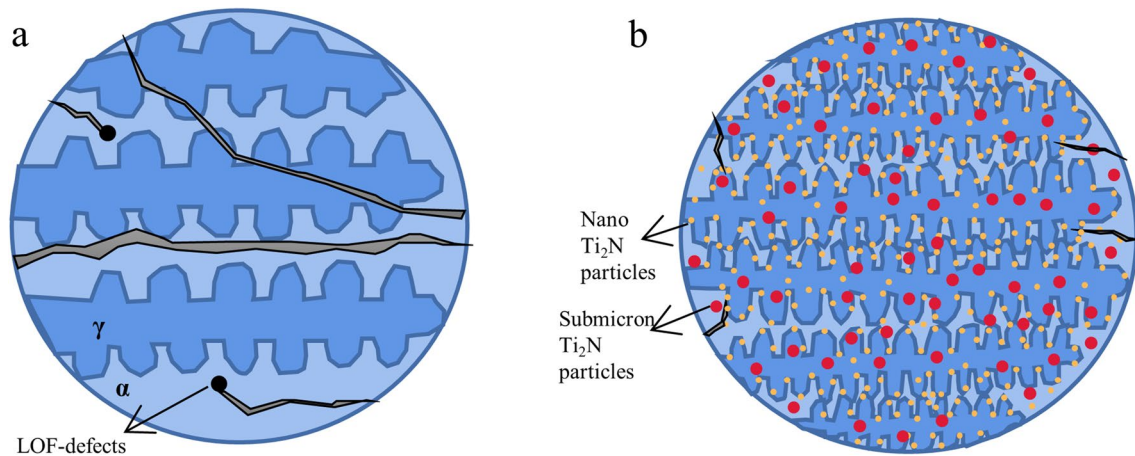
Fig. 15 The tensile fracture mechanisms of the LMDed samples. **a** Samples without Ti_2N; **b** Samples with nano and submicron Ti_2N

Generally speaking, for particles reinforced iron-matrix composites, plastic deformation was stopped at the interface between the matrix and the particles, causing stress concentrations and limiting ductility [36]. But in this study, during the loading process, the uniform distribution of nano and submicron Ti_2N particles (Fig. 6c–d) contributed to transfer the stress homogeneously and reduced or even avoided the stress concentration. And the particles with the large specific surface area and higher surface energy led to the higher dislocation density around the particles and eventually improved the material elongation [37]. Furthermore, the nano Ti_2N particles pinned at the grain boundaries (Fig. 7d–e) to impede grain growth, and the submicron Ti_2N particles supplied effective heterogeneous nucleation to refine the grains. Grain refinement (according to the grain size in Fig. 5e–j) resulted in more numbers of grains, and deformation scattered in more grains under the same conditions, leading to the improvement of deformation uniformity. Meantime, the number of the grain boundaries increased and the boundaries became more tortuous due to the grain refinement (Fig. 5c–d), which could effectively suppressed crack extension [36] (Fig. 15b). The nano Ti_2N particles partially at the grain boundaries (Fig. 7d–e) altered the path of crack growth (Fig. 15b), resulting in crack branching and deflection, which enhanced the crack extension resistance [38]. Therefore, the nano and submicron Ti_2N particles dispersed in the matrix simultaneously improved the strength and plasticity of the composite material, thereby providing the toughening effect.

Finally, the volume ratio of ferrite and austenite increased from 43:57 (SAF2906-3Mo) to 28:72 (SAF2906-2TiN) and 21:79 (SAF2909-4TiN) with the increase of TiN addition, respectively, shown in Fig. 3b. Compared with ferrite, austenite has better ductility, so the increase of austenite content contributed to improve the elongation of DSS. The

combination of the above factors led to a significant increase in the plasticity of SAF2906-2TiN and SAF2906-4TiN.

3.2.3 Corrosion Resistance

The Tafel curves of the LMDed samples with different molybdenum contents and nano TiN additions in the simulated phosphoric acid slurry solution were shown in Fig. 16. The samples were all passivated during the anodic polarization process. Table 9 listed the parameters of Tafel curves, including self-corrosion potential (E_{corr}), self-corrosion current density (I_{corr}), Tafel slope (β_c and β_a) and polarization resistance (R_p), where the polarization resistance was obtained by formula (3). The more positive the E_{corr} was, the lower the corrosion tendency was, and the more difficult it was to be corroded. When
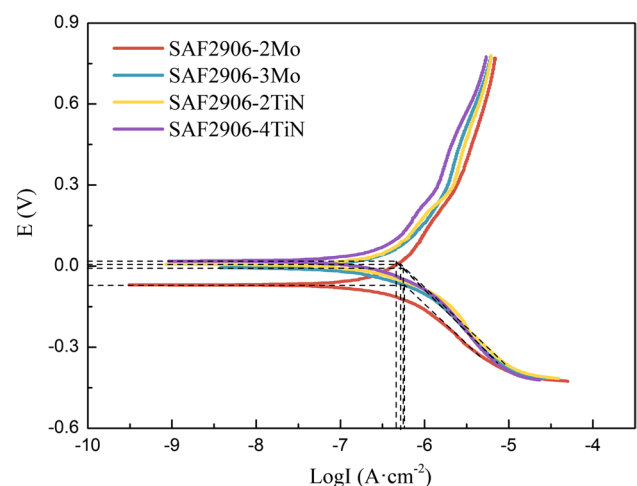

Fig. 16 The Tafel curves of the LMDed samples with different molybdenum contents and nano TiN additions in the simulated phosphoric acid slurry solution

Table 9 The Tafel results of the LMDed samples with different molybdenum contents and nano TiN additions

Samples	E_{corr}/V	I_{corr}/(A·cm^{-2})	β_c/(V·dec^{-1})	β_a/(V·dec^{-1})	R_p/(Ω·cm^2)
SAF2906-2Mo	− 0.0690	5.75×10^{-7}	0.30	0.78	163,831
SAF2906-3Mo	− 0.0057	5.49×10^{-7}	0.36	0.88	202,331
SAF2906-2TiN	0.0096	5.12×10^{-7}	0.35	0.84	209,798
SAF2906-4TiN	0.0216	4.57×10^{-7}	0.36	0.86	241,433

the R_p was greater, the reaction resistance was greater, and the corrosion rate was smaller, which meant that it was more difficult to be corroded. The smaller the I_{corr} was, the smaller the corrosion rate was, and the better the corrosion resistance was.

$$R_p = \frac{\beta_a \times \beta_c}{2.3 \times I_{corr} \times (\beta_a + \beta_c)} \qquad (3)$$

As the molybdenum content increased from 2 to 3 wt%, the E_{corr} rose from − 0.0690 to − 0.0057 V, while the I_{corr} decreased from 5.75×10^{-7} to 5.49×10^{-7} A·cm^{-2}. Simultaneously, the R_p increased from 163,831 to 202,331 Ω·cm^2, indicating that the corrosion rate declined and the samples were more difficult to be corroded.

The E_{corr} gradually ascended from -0.0057 V (SAF2906-3Mo) to 0.0096 V (SAF2906-2TiN) and 0.0216 V (SAF2906-4TiN), and the I_{corr} continuously descended from 5.49×10^{-7} A·cm^{-2} (SAF2906-3Mo) to 5.12×10^{-7} A·cm^{-2} (SAF2906-2TiN) and 4.57×10^{-7} A·cm^{-2} (SAF2906-4TiN). The E_{corr} of SAF2906-3Mo and SAF2906-2TiN were similar, slightly lower than that of the SAF2906-4TiN sample. The R_p of SAF2906-2TiN (209,798 Ω·cm^2) and SAF2906-4TiN (241,433 Ω·cm^2) were obviously larger than that of SAF2906-3Mo (202,331 Ω·cm^2). Thereby the corrosion resistance was improved when the TiN addition increased.

Electrochemical impedance tests were carried out on the LMDed samples with different molybdenum contents and nano TiN additions in simulated phosphoric acid slurry solution. The electrochemical impedance spectroscopy (EIS) data and equivalent circuit model of the LMDed SAF2906 were obtained as shown in Fig. 17. According to Fig. 17a, the capacitive arc radius of the Nyquist diagram was used to characterize the corrosion resistance of the material. The capacitive arc radius of SAF2906-3Mo was obviously larger than that of SAF2906-2Mo, showing the greater dissolution resistance of the material surface and better corrosion resistance. The capacitive arc radius of SAF2906-2TiN slightly ascended compared with SAF2906-3Mo, while the radius of SAF2906-4TiN was much larger than that of SAF2906-3Mo and SAF2906-2TiN, and the corrosion resistance was the best. According to Fig. 17c, in the low frequency region, the impedance modulus of the samples with TiN was greater than that

of the samples without TiN, and SAF2906-4TiN showed the greatest impedance modulus, which further confirmed that the corrosion resistance was improved after TiN was added to the DSS.

According to Fig. 17a–b, all samples showed the similar EIS characteristics. Only one peak in phase angle plots and only one semicircle capacitive arc with the center in the fourth quadrant in Nyquist diagram, that was, there was only one time constant in the electrochemical reaction. The equivalent circuit model was used to fit the impedance spectrum as shown in Fig. 17d, and the EIS parameters for stainless steel in phosphoric acid slurry solution were listed in Table 10. R_s represented the solution resistance, and R_{ct} was the charge transfer resistance. CPE was the electric double layer capacitance, which was usually used to describe the non-ideal capacitive behavior due to the surface non-uniformity, roughness or fractal geometry, electrode porosity, and uneven distribution of current and potential [39]. n was the dispersion factor, which was always between 0.5 and 1. When $n = 1$, CPE showed an ideal capacitive behavior; when $n = 0.5$, CPE showed the Warburg impedance behavior; for $0.5 < n < 1$, CPE represented non-ideal behavior as a constant phase element [40].

In this experiment, the dispersion factor n was about 0.9, indicating that the electrode surface was relatively smooth and the corrosion product film was dense and uniform. The value of R_s was basically the same, showing that the system was in a relatively stable state for each test. On the premise of the similar R_s values, the greater the R_{ct} value was, the greater the resistance of the sample surface was, which made the I_{corr} of the material smaller and the final corrosion resistance better. The R_{ct} of SAF2906-3Mo (106,770 Ω·cm^2) was larger than that of SAF2906-2Mo (83,267 Ω·cm^2), and the corrosion resistance was improved by increasing the molybdenum content. After adding nano TiN to the samples, the R_{ct} value increased greatly. The R_{ct} of SAF2906-2TiN was 114,640 Ω·cm^2, while the R_{ct} of SAF2906-4TiN was 164,190 Ω·cm^2, which possessed the best corrosion resistance in the LMDed samples.

According to the research of Wu [41] and Moon [42], it can be speculated that in the simulated phosphoric acid slurry solution of this experiment, the samples containing molybdenum formed a passivation film containing MoO_3 on the surface of the stainless steel, which strengthened and thickened the Cr_2O_3 passivation film on the surface of the
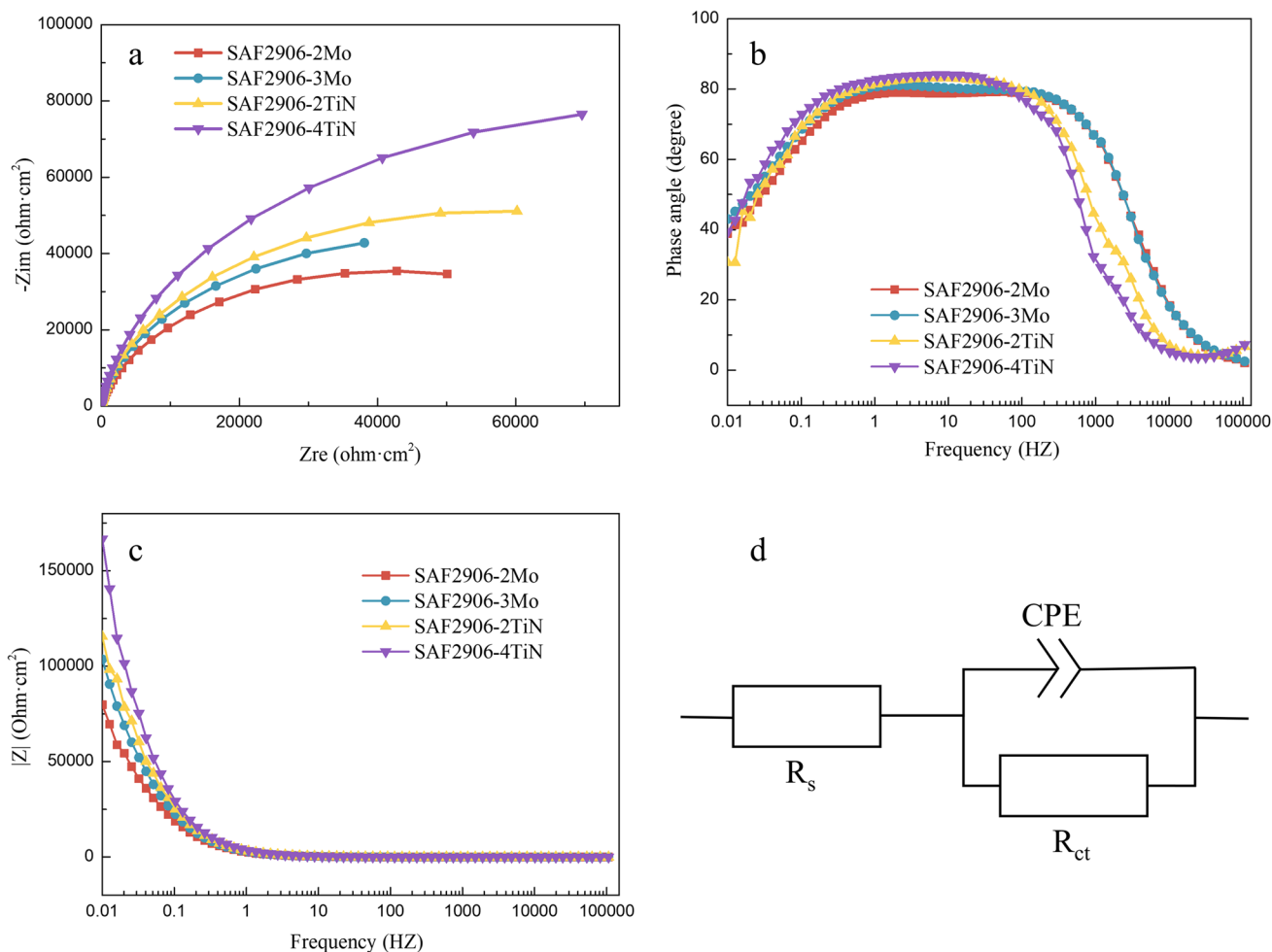
Fig. 17 EIS data and equivalent circuit model of the LMDed samples with different molybdenum contents and nano TiN additions. **a** Nyquist diagram; **b** Phase angle plots; **c** Bode impedance; **d** Equivalent circuit

Table 10 EIS parameters for stainless steel in phosphoric acid slurry solution

Samples	$R_{ct}/(\Omega \cdot cm^2)$	$R_s/(\Omega \cdot cm^2)$	CPE/ $(\Omega^{-1} \cdot s^{-n} \cdot cm^{-2})$	n
SAF2906-2Mo	83,267	1.921	7.26×10^{-5}	0.89
SAF2906-3Mo	106,770	1.959	6.25×10^{-5}	0.91
SAF2906-2TiN	114,640	2.724	5.55×10^{-5}	0.93
SAF2906-4TiN	164,190	2.361	4.88×10^{-5}	0.94

stainless steel. The presence of molybdenum in the passivation film also promoted the enrichment of chromium, and improved the passivation ability of stainless steel, enhancing the corrosion resistance. After adding nano TiN to the SAF2906-3Mo sample, part of nitrogen was dissolved in the stainless steel matrix. In the simulated phosphoric acid slurry solution, according to the research of Luiz [43], nitrogen combined with H^+ in the passivation film to form NH_3 and NH_4^+. These reactions prevented localized acidification and improved localized corrosion resistance. The coexistence of molybdenum and nitrogen led to a synergistic effect of the protective mechanism. However, pitting corrosion occurred preferentially at the interface between in-situ formed Ti_2N particles and the matrix, so the matrix became the anode and microgalvanic corrosion occurred [27, 44]. The combined effects of these factors made the corrosion resistance of the samples with nano TiN addition improved.

4 Conclusion

In this paper, SAF2906 duplex stainless steel was fabricated by powder prepasted laser melting deposition. The molybdenum content was adjusted to balance the volume ratio of ferrite and austenite, and the effects of the nano TiN addition on the microstructure evolution and properties of the duplex stainless steel were studied.

(1) The LMDed SAF2906 DSS consisted of austenite and ferrite. The molybdenum content was increased from 2 to 3 wt% to obtain balanced volume ratio of ferrite and austenite (4:6). The nano TiN particles melted and nano (10–100 nm) and submicron (100 nm ~ 1 μm) Ti_2N particles were generated in situ. Ti_2N particles were uniformly distributed in the DSS matrix, and some nano Ti_2N particles preferred to be distributed at grain boundaries. The primary and secondary dendrite spacing of austenite of LMDed SAF2906 with 4wt% TiN addition reduced by 48% and 62%, respectively, and the austenite content ascended by 15%.

(2) When Mo content rose from 2 to 3 wt%, the wear resistance (with wear rate from 1.77×10^{-12} to 1.28×10^{-12} m^3/Nm) of stainless steel was enhanced, and the corrosion resistance (with self-corrosion potential and self-corrosion current density from -0.0690 V and 5.75×10^{-7} A·cm^{-2} to -0.0057 V and 5.49×10^{-7} A·cm^{-2}) was also improved.

(3) With the nano TiN addition of 4 wt%, the average microhardness of composites (381 HV$_{0.2}$) increased by 17% compared to SAF2906-3Mo (326 HV$_{0.2}$), and the wear rate (9.12×10^{-13} m^3/Nm) was only 71% that of SAF2906-3Mo (1.28×10^{-12} m^3/Nm). The yield strength, tensile strength and elongation ascended from 700 MPa, 885 MPa and 16.9% (SAF2906-3Mo) to 801 MPa, 1028 MPa and 31.8%(SAF2906-4TiN), respectively. The self-corrosion potential of SAF2906-4TiN increased to 0.0216 V, and the self-corrosion current density was also minimum 4.57×10^{-7} A•cm^{-2}, indicating the advance of corrosion resistance.

Author Contributions SY: Conceptualization, Methodology, Investigation, Formal analysis, Writing—original draft. JL: Supervision, Project administration, Resources, Funding acquisition. YL: Investigation. XY: Writing—review & editing. SC: Resources. CL: Supervision, Funding acquisition.

Declarations

Conflict of interest The authors declare that they have no known competing financial interests or personal relationships that could have appeared to influence the work reported in this paper.

References

1. A.E. Odermatt, V. Ventzke, F. Dorn, R. Dinsé, P. Merhof, N. Kashaev, J. Manuf. Process. **72**, 148–158 (2021)

2. F. Khoshnaw, C. Marinescu, A. Sofronia, C. Munteanu, M. Marcu, L.E. Barbulescu, C. Ciobota, E.M. Cojocaru, S. Tanasescu, A. Paraschiv, Mater. Today Commun. **28**, 102644 (2021)

3. G. Fargas, A. Mestra, A. Mateo, Wear **303**, 584–590 (2013)

4. K. Saeidi, L. Kevetkova, F. Lofaj, Z. Shen, Mater. Sci. Eng. A **665**, 59–65 (2016)

5. Y. Zhang, W. Huang, J. Manuf. Process. **57**, 324–333 (2020)

6. D. Abolhasani, S.M. Hossein Seyedkashi, T.W. Hwang, Y.H. Moon, Mater. Sci. Eng. A **763**, 138161 (2019)

7. P. Xu, C. Lin, C. Zhou, X. Yi, Surf. Coat. Tech. **238**, 9–14 (2014)

8. M. Rashkovets, M. Mazzarisi, A.A. Nikulina, G. Casalino, Mater. Lett. **274**, 128064 (2020)

9. K. Zhang, S. Wang, W. Liu, X. Shang, Mater. Des. **55**, 104–119 (2014)

10. Z. Sun, X. Tan, S.B. Tor, W.Y. Yeong, Mater. Des. **104**, 197–204 (2016)

11. J. Liang, Z.Y. Lin, X.Y. Yin, S.Y. Chen, C.S. Liu, R.H. Chai, H.W. Zhang, G.Q. Tang, K. Tian, Met. Mater. Int. **28**, 216–226 (2022)

12. J.H. Jang, B.D. Joo, C.J. Van Tyne, Y.H. Moon, Met. Mater. Int. **19**, 497–506 (2013)

13. F. Hengsbach, P. Koppa, K. Duschik, M.J. Holzweissig, M. Burns, J. Nellesen, W. Tillmann, T. Tröster, K.-P. Hoyer, M. Schaper, Mater. Des. **133**, 136–142 (2017)

14. K.P. Davidson, S.B. Singamneni, Rapid Prototyp. J. **23**, 1146–1163 (2017)

15. G. Posch, K. Chladil, H. Chladil, Weld World **61**, 873–882 (2017)

16. E. Kennedy, B.S. Sachin, M. Ramachandra, C.A. Niranjan, N. Sriraman, V.K.S. Jain, N. Sathiya Narayanan, Mater. Today Proc. **39**, 1710–1713 (2021)

17. C.-W. Chan, J. Quinn, I. Hussain, L. Carson, G.C. Smith, S. Lee, Surf. Coat. Tech. **405**, 126714 (2021)

18. X. Wang, Z. Zhang, Y. Men, X. Li, Y. Liang, L. Ren, Opt. Laser Technol. **126**, 106136 (2020)

19. D. Zhou, F. Qiu, Q. Jiang, Mater. Sci. Eng. A **596**, 98–102 (2014)

20. C. Gao, Z. Xiao, Z. Liu, Q. Zhu, W. Zhang, Mater. Lett. **236**, 362–365 (2019)

21. Y. Wang, Z. Liu, Y. Zhou, X. Yang, J. Tang, X. Liu, J. Li, G. Le, Mater. Sci. Eng. A **814**, 141220 (2021)

22. S.R. Oke, M.R. Mphahlele, O.O. Ige, O.E. Falodun, A.M. Okoro, P.A. Olubambi, J. Alloys Compd. **840**, 155648 (2020)

23. S.R. Oke, O.O. Ige, O.E. Falodun, B.A. Obadele, M.R. Mphahlele, P.A. Olubambi, Mater. Chem. Phys. **206**, 166–173 (2018)

24. S.R. Oke, O.O. Ige, O.E. Falodun, P.A. Olubambi, J. Westraadt, Int. J. Refract. Met. Hard Mater. **81**, 78–84 (2019)

25. S.R. Oke, O.O. Ige, O.E. Falodun, B.A. Obadele, M.B. Shongwe, P.A. Olubambi, J. Mater. Res. Technol. **7**, 126–134 (2018)

26. O.O. Ige, S.R. Oke, O.E. Falodun, S. Aribo, K.M. Oluwasegun, O.O. Ajibola, J.O. Olawale, A. Ogunbadejo, O.T. Olalemi, P.A. Olubambi, Mater. Today: Proc. **38**, 688–695 (2021)

27. S. Olukayode Akinwamide, O. Jeremiah Akinride, M. Mafafo, M. Phumlani, B. Abiodun Obadele, B. Tolulope Abe, P. Apata Olubambi, Mater. Today Proc. **28**, 384–387 (2020)

28. C. Zhang, S. Chen, L. Zhou, M. Wei, J. Liang, C. Liu, M. Wang, J. Manuf. Process. **62**, 337–347 (2021)

29. M. Wei, S. Chen, M. Sun, J. Liang, C. Liu, M. Wang, Mater. Charact. **160**, 110097 (2020)

30. P. Zuo, S. Chen, M. Wei, L. Zhou, J. Liang, C. Liu, M. Wang, J. Manuf. Process. **44**, 28–37 (2019)

31. G.M. Karthik, H.S. Kim, Met. Mater. Int. **27**, 1–39 (2021)

32. Y. Liu, Z. Long, H. Wang, Y. Du, B. Huang, Scr. Mater. **55**, 367–370 (2006)

33. L. Huang, X. Deng, Q. Wang, Y. Jia, C. Li, Z. Wang, Wear **458–459**, 203444 (2020)

34. D.V. Isquierdo, R.H.M. Siqueira, S.M. Carvalho, M.S.F. Lima, J. Mater. Res. Technol. **18**, 5267–5279 (2022)

35. D. D. Gu, Y. Yang, L. X. Xi, J. K. Yang and M. J. Xia, Opt. Laser Technol. **119** (2019).
36. K. Xie, J. Nie, X. Ma, X. Liu, Mater. Charact. **170**, 110672 (2020)
37. X. Niu, G. Li, Z. Zhang, P. Zhou, H. Wang, S. Zhang, W. Cheng, Mater. Sci. Eng. A **743**, 207–216 (2019)
38. B. Gao, H. Peng, Y. Liang, J. Lin, B. Chen, Mater. Sci. Eng. A **811**, 141059 (2021)
39. T. Zhu, X. Gong, Y. Xiong, X. Hu, Met. Mater. Int. **27**, 2645–2655 (2021)
40. A.M. Santos, I.P. Aquino, F. Cotting, I.V. Aoki, H.G. de Melo, V.R. Capelossi, Met. Mater. Int. **27**, 1519–1530 (2021)
41. H. Wu, S. Zhang, Z.Y. Wang, C.H. Zhang, H.T. Chen, J. Chen, Int. J. Refract. Met. Hard Mater. **102**, 105721 (2022)
42. J. Moon, H.-Y. Ha, S.-J. Park, T.-H. Lee, J.H. Jang, C.-H. Lee, H.N. Han, H.-U. Hong, J. Alloys Compd. **775**, 1136–1146 (2019)
43. L.A. Luiz, B.C.E.S. Kurelo, G.B.D. Souza, J.D. Andrade, C.E.B. Marino, Mater. Today Commun. **28**, 102655 (2021)
44. M.B. Leban, R. Tisu, Eng. Fail. Anal. **33**, 430–438 (2013)